Applied Catalysis B: Environmental 343 (2024) 123502

Contents lists available at ScienceDirect

Applied Catalysis B: Environmental

journal homepage: www.elsevier.com/locate/apcatb

Interfacial synergistic effect of Ru nanoparticles embedded onto amorphous/crystalline WO_3 nanorods on boosting the pH-universal hydrogen evolution reaction

Jialin Cai [a,b], Wenlei Zhang [a], Yanyan Liu [c], Ruofan Shen [a], Xin Xie [a], Wanyu Tian [a], Xingang Zhang [a], Jie Ding [a,*], Yushan Liu [a,*], Baojun Li [a,*]

[a] The Green Catalysis Center, College of Chemistry, Zhengzhou University, 100 Science Road, Zhengzhou 450001, PR China
[b] College of Material, Henan Key Laboratory of Aeronautical Materials and Application Technology, Zhengzhou University of Aeronautics, Zhengzhou 450046, PR China
[c] College of Science, Henan Agricultural University, 63 Nongye Road, Zhengzhou 450002, PR China

ARTICLE INFO

Keywords:
Solid-phase reaction
Amorphous/crystalline WO_3
Oxygen vacancy
PH-universal
Hydrogen evolution reaction

ABSTRACT

The development of high-efficiency pH-universal electrocatalyst is of great significance for hydrogen evolution reaction (HER). In this work, a rod-like Ru/WO_3-V_O electrocatalyst was constructed for HER via a solid-phase reaction strategy. Due to the restriction of atomic migration at solid phase interface, plenty of oxygen vacancies (V_O) and structure distortions were generated in amorphous/crystalline WO_3 phase (WO_3-V_O). The optimized Ru/WO_3-V_O annealed at 450 °C with 2.2 *wt*% Ru achieves outstanding intrinsic activity with low overpotential and Tafel slope in a 0–14 pH range. A turnover frequency value 7.2 higher than that of commercial Pt/C is abtaind on Ru/WO_3-V_O at overpotential of 100 mV. Density functional theory calculations reveal that H* adsorption and desorption balanced by tuning the interface electronic structure contributes synergistic effect to the pH-universal HER activity of Ru/WO_3-V_O. The crystalline/amorphous semiconductor-metal heterointerface is crucial to designing and synthesizing electrocatalysts for optimal HER activity.

1. Introduction

Nowadays, the exploration of high-efficient catalyst is indispensable for the harvest, conversion and storage of sustainable energy [1–3]. In a typical electrochemical hydrogen evolution reaction (HER) process, the different proton-electron coupling mechanism at changing pH value on the surface of cathode limited the overall activity of catalyst [4]. Alternatively, the pH-independent catalysts can work efficiently and maintain their catalytic activity and stability under various pH conditions, including alkaline, acidic, and neutral environments. Meanwhile, pH-independent catalysts are generally stronger and more resistant to degradation, which can effectively simplify system design, reduce operational complexity, and reduce maintenance cost [2,3]. Therefore, high-efficiency HER electrocatalyst over a wide pH range is urgently needed [5,6]. Amorphous materials with abundant defect structure, diverse chemical compositions, and benign structural flexibility display great potential as HER catalysts [7,8]. But the amorphous structure still suffers from inherently poor electrical conductivity and low stability [9,10]. As a counterpart to amorphous materials, the crystalline phase owns the advantages of high electrical conductivity, definite structure, and remarkable corrosion resistance [11–13]. Through combining the structural advantages of amorphous and crystalline phases, crystalline-amorphous heterojunctions have been proven as an effective means to enhance the efficiency of hydrogen evolution over a wide pH range [14–18]. In case of TMOs, ordered atomic arrangements in crystalline structures can contribute high electric conductivity and strong stability. In amorphous structures containing short-range disordered atoms arrangement, tremendous of structural distortions and unsaturated coordination atoms can induce new active sites [19,20]. Therefore, crystalline/amorphous hetero-structured TMOs with the advantages of conductive crystalline phase and catalytically active amorphous phase is a more suitable choice for promoting HER performance of electrocatalyst over a wide pH range.

As a layered binary crystalline transition metal oxides (TMOs), tungsten trioxide (WO_3) present high conductivity and strong electrochemical durability in HER [21–24]. In amorphous WO_3, there are many oxygen vacancies (V_O) and low-valent W species embedded in lattice [25,26]. Especially, as a shallow electron donor, surface V_O can promote

* Corresponding authors.
E-mail addresses: jieding@zzu.edu.cn (J. Ding), liuyushan@zzu.edu.cn (Y. Liu), lbjfcl@zzu.edu.cn (B. Li).

https://doi.org/10.1016/j.apcatb.2023.123502
Received 14 May 2023; Received in revised form 3 November 2023; Accepted 9 November 2023
Available online 11 November 2023
0926-3373/© 2023 Elsevier B.V. All rights reserved.

total electrocatalytic activity by influencing adhesion effect and electronic structure of support and active materials [27]. An amorphous/crystalline heterostructures will introduce a certain amount of oxygen vacancy defects into WO_3 through interface engineering [27–29]. Oxygen vacancies work via constructing more active sites to improve the efficiency of TMOs in hydrogen evolution [25,26]. Due to the strong metal-support interaction, the hybridization of Ru nanoparticles (NPs) with TMOs can enhance the stability of Ru component and the total catalytic activity of material to become favorable candidate [30–32]. In previous works, a solid-phase reaction (SPR) strategy paves an effective way to coupling metal NPs and V_O together onto the surface of TMOs [33]. In the SPR strategy, the phase transformation of components can be conveniently modurated by reaction kinetics. Furthermore, the unique substance diffusion behavior during the SPR process drives the formation and modulation amorphous/crystalline heterostructure. Rational assemble of amorphous and crystalline phases is an attractive method to tunate V_O density of WO_3 and further achieves the optimization of surface chemical property and *d*-band center in Ru-WO_3 hybrid material. There are still challenge in the controllable construction of morphous/crystalline heterostructure with definite structure by the SPR strategy.

Herein, we report an efficient Ru/WO_3-V_O electrocatalyst for HER constructed by an SPR strategy. Based on the phase transition from amorphous to crystalline during the SPR strategy reaction process, the crystalline and amorphous heterojunction structure was obtained. From rod-like RuO_2/WC precursor, RuO_2 NPs and WC nanorods were successfully transformed into Ru NPs and V_O-rich amorphous/crystalline WO_3 phase (WO_3-V_O), respectively. Experiments demonstrate that rod-like WO_3-V_O effectively accelerate charge transport and reduces severely agglomeration of Ru NPs during HER process. Ru/WO_3-V_O electrocatalyst exhibited outstanding performance and excellent stability in a wide pH range. Density functional theory (DFT) calculations reveal the synergistic effect between different active sites in the Ru/WO_3-V_O electrocatalyst. This research can contribute to the development of sustainable energy based on the HER catalysis.

2. Experimental section

2.1. Chemicals

Sulfuric acid (H_2SO_4), ethanol, and potassium hydroxide (KOH) were analytical reagents, which were purchased from Tianjin Fengchuan Chemical Reagent Technologies Co., Ltd. Ammonium tungsten partial ($H_{28}N_6O_{41}W_{12}$), Sodium sulfocyanate (NaSCN), sodium chloride (NaCl), polyvinyl pyrrolidone (PVP, K-17), and hydrogen peroxide (H_2O_2, ≥ 30 %), calcium hydroxide ($Ca(OH)_2$) were provided by Sinopharm Chemical Reagent Co. Ltd. Ruthenium (III) chloride hydrate ($RuCl_3 \bullet nH_2O$, ~37 wt%) was received from Kunming Institute of Precious Metals. Nafion membrane (5 wt% in lower aliphatic alcohols and water) was purchased from Aldrich Co. Ltd., and Pt/C (20 wt%) was provided by Aladdin. The commercial Ru/C (5 wt%) was bought from Aladdin. All of the chemical reagents were analytical grade and used directly without any further purification. Deionized water. All chemical reagents were purchased from commercial suppliers and used without further purification.

2.2. Preparation of rod-like-WC

In a typical synthesis, 1.0 g of polyvinylpyrrolidone, 1 g of Ammonium tungsten partial and 1.2 g of NaCl were first dissolved in 50 mL of distilled water under magnetic stirring for 30 min to form a homogeneous solution. Then, the solution was treated with liquid nitrogen rapidly and further freeze-dried for 1 day at –40 °C with a pressure of 1 Pa to yield a precursor. The as-prepared W-containing precursor was mildly annealed in a tube resistance furnace at 800 °C for 4 h in an N_2 atmosphere. After being cooled to room temperature, rod-like -WC was obtained after removing the NaCl by using deionized water.

2.3. Preparation of WC dispersion solution

Typically, 0.22 g WC was dispersed into 40 mL distilled water and ultrasonicated via ultrasonic cell disruption for 2 h in an ice bath to obtain a well-dispersion liquid.

Preparation of RuO_2/WC and Ru/WO_3-V_O. 3.5 mL $RuCl_3 \cdot xH_2O$ solution (10 mg mL^{-1}) dropped wisely and added into the 40 mL WC dispersion. Subsequently, a diluted H_2O_2 solution (a 30 % aqueous H_2O_2 solution was mixed with 20 mL H_2O) was added into the mixture, which was further transferred to a 100 mL Teflon-lined autoclave and heated to 95 °C in 5 h. After the cooling process, the product was collected by centrifugation and washing. The prepared RuO_2/WC composite was dried in a vacuum oven at 60 °C for 12 h. Finally, the precursor RuO_2/WC was heated at 450 °C for 6 h under Ar atmosphere to obtain the final product (Ru/WO_3-V_O). The content of Ru metal in Ru/WO_3-V_O was 2.2 *wt*% by ICP-AES. The samples of WC-X $RuCl_3 \cdot xH_2O$ (x = 25, 35, 45, and 55 mg, and X stands for the mass of the $RuCl_3 \cdot xH_2O$ used) were also prepared by simply changing the mass of the $RuCl_3 \cdot xH_2O$. For comparison, RuO_2/WC was heated under different temperature conditions. The resulting product was denoted as Ru/WO_x-T, and T represents the annealing temperature.

2.4. Characterization

The samples were identified and characterized by X-ray powder diffraction (XRD) analysis system (Bruker, Model D8 Advance) and X-ray photoelectron spectroscopy (XPS) (Thermo Fisher, Model ESCALAB 250Xi), respectively. The detailed structures of samples were revealed by scanning electron microscope (SEM) analysis (JEOL, Model JSM-6301F). The material morphologies were studied by using transmission electron microscope (TEM, FEI Tecnai G^2 F20 S-TWIN, operating at 200 kV), combined with energy-dispersive X-ray spectroscopy (EDX). Sub-angstrom resolution HAADF-STEM images were obtained on a FEI equipped (Themis Z) probe corrector, operating at 300 kV. TGA analysis was carried out using a TGA system (Netzsch, Model STA 449 F3) in N_2 atmosphere with a constant heating rate of 10 °C min^{-1} from 30 to 600 °C. The chemical composition of the catalysts was analyzed by inductively coupled plasma atomic emission spectroscopy (ICP-AES) using a thermo ICAP6000 SERIES. The electron paramagnetic resonance (EPR) spectra were obtained using a Bruker A300 EPR spectrometer at X-band (≈9 GHz) at low temperature. The gas product was performed using a gas chromatograph (GC, PANNA A91PLUS). The X-ray absorption fine structure spectra were collected at BL14W beamline in Shanghai Synchrotron Radiation Facility (SSRF). The storage rings of SSRF was operated at 3.5 GeV with a stable current of 200 mA. Using Si (111) double-crystal monochromator, the data collection was carried out in transmission mode using Lytle detector.

2.5. Electrochemical measurements

Electrochemical measurements were performed in a three-electrode system with an electrochemical workstation (CHI-760E) in the acidic (0.5 M H_2SO_4), alkaline (1 M KOH) and neutral (1 M PBS) electrolyte, respectively. Carbon stick and calomel (saturated KCl, SCE) were used as the counter and reference electrode, respectively. The as-prepared sample was loaded on a glassy carbon electrode to form the working electrode. All potentials were calibrated by the reversible hydrogen electrode (RHE, $E_{RHE} = E_{SCE} + 0.241 + 0.0591$ pH). Typically, 3 mg sample powder was dispersed in a mixed solvent (500 μL ethanol with 50 μL Nafion solution). Subsequently, 10 μL (loading ~0.28 mg cm^{-2}) dispersion was loaded on the glassy-carbon disk by a drop-cast method. The linear sweep voltammetry (LSV) was collected at a scan rate of 2 mV s^{-1} for the HER. The EIS was measured at 10 mA cm^{-2} in the region of 0.1–10^5 Hz with an amplitude of 5 mV. The capacitance of

electrochemical double-layer (C_{dl}) of various samples was estimated using the cyclic voltammetry (CV) test at an interval of non-faradic process in a small potential range (ΔU = 0.1 V). Besides, The CV curves were acquired at the scan rate from 5 to 45 mV s^{-1}. The long term stability test was carried out by repetitive CV scans at a sweep rate of 50 mV s^{-1}. All the tests were performed without iR-corrections. The *TOF* of Ru/WO_3-V_O was compared to that of commercial 20 % Pt/C in 1 M KOH at varied kinds of voltage. The TOF value was calculated based on the active sites density of the catalysts by the following equation: $TOF = I/(2nF)$ where I is the current intensity at a given overpotential on the LSV measurement, F is the Faradaic constant, and n is the number of active sites. The factor 1/2 is based on the consideration that two electrons are required to form one hydrogen molecule. Faraday efficiency = (number of mole of measured H_2)/(number of mole of theoretical H_2)× 100 %.

2.6. Computational method

The first-principles was employed to perform all the density functional theory (DFT) calculations within the generalized gradient approximation (GGA) using the Perdew, Burke, and Enzerhof (PBE) functional. The projected augmented wave (PAW) potentials were applied to describe the ionic cores and take valence electrons into account using a plane wave basis set with a kinetic energy cutoff of 450 eV. Partial occupancies of the Kohn–Sham orbitals were allowed using the Gaussian smearing method and a width of 0.05 eV. The electronic energy was considered self-consistent when the energy change was smaller than 10^{-4} eV. A geometry optimization was considered convergent when the force change was smaller than 0.05 eV/Å. Grimme's DFT-D3 methodology was used to describe the dispersion interactions. The equilibrium lattice constants of unit cell were optimized when using a 5 × 5 × 5 Monkhorst-Pack k-point grid for Brillouin zone sampling. And the surface (WO_3 (0 2 2)) had been used the 2 × 2 × 1 Monkhorst-Pack k-point. In addition, the density of states had been investigated using 3 × 3 × 1 Monkhorst-Pack scheme k-point mesh for the structures. The free energy is calculated as follows: G=E + ZPE-TS. where G, E, ZPE and TS are the free energy, total energy from DFT calculations, zero point energy and entropic contributions, respectively. The U correction had been used in our structures for metal atoms.

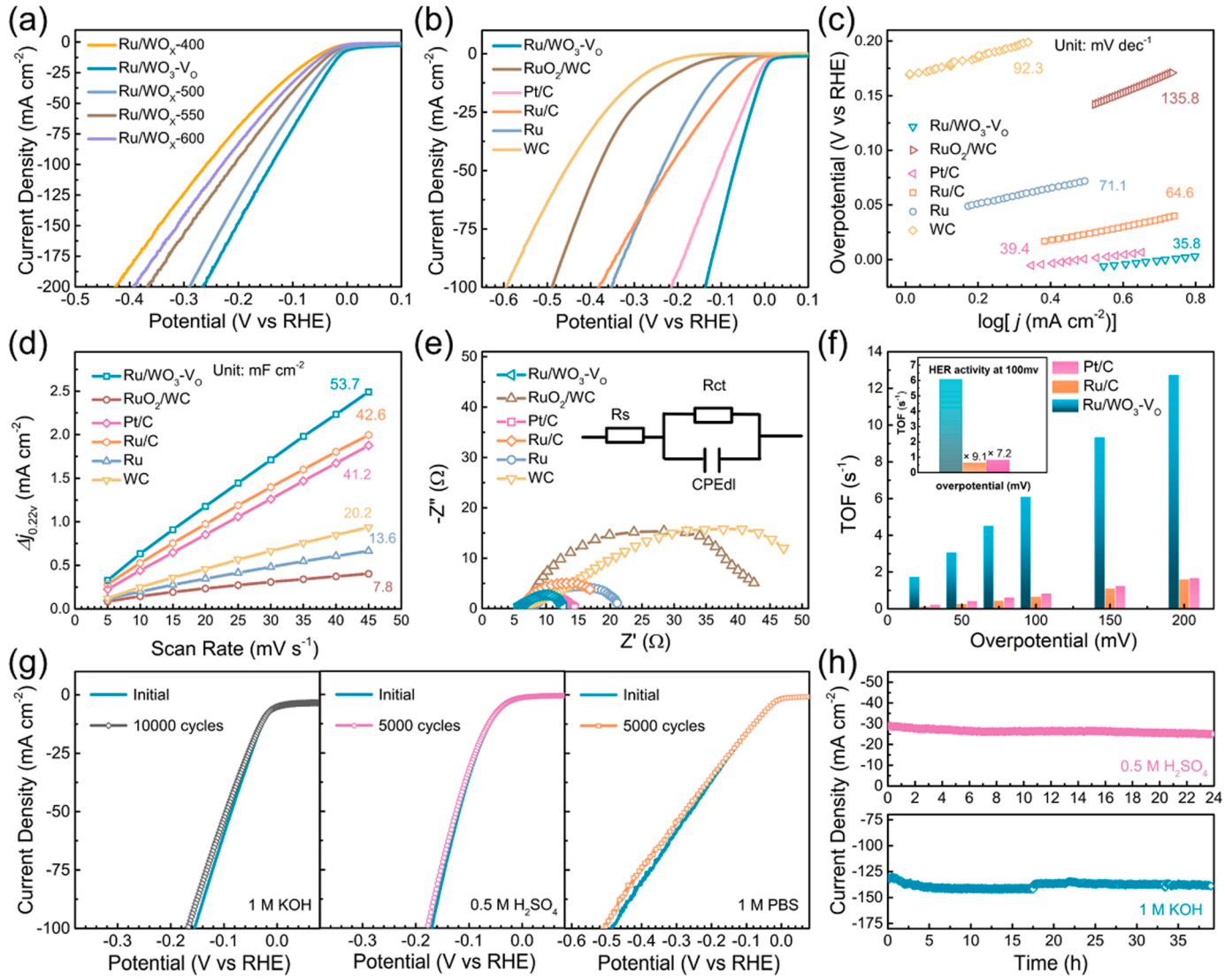

Fig. 1. (a) HER polarization curves of RuO_2/WC samples annealed at different temperatures. (b) HER polarization curves. (c) corresponding Tafel plots. (d) capacitive current at middle potential of CV curves as a function of scan rates to fit linear regression. (e) Nyquist plots of Ru/WO_3-V_O, commercial Pt/C (20 %), commercial Ru/C (5 %), WC, Ru/C, and RuO_2/WC. (f) TOF of Ru/WO_3-V_O, Ru/C, and Pt/C at varied kinds of voltage. (a–f) were tested in 1 M KOH. (g) Polarization curves of Ru/WO_3-V_O after different cycles at different pH values. (h) stable operation of Ru/WO_3-V_O in 1 M KOH and 0.5 M H_2SO_4.

3. Results and discussion

3.1. Catalytic performances

To determine the electrocatalytic property of Ru/WO_3-V_O, HER polarization curves were obtained in 1 M KOH electrolyte. In Fig. 1a, Ru/WO_3-V_O required a very low overpotential of 10 mV to achieve the current density of 10 mA cm^{-2}. Compared that on Ru/WO_3-V_O, the HER on Ru/WO_x-400 (41 mV), Ru/WO_x-500 (21 mV), Ru/WO_x-550 (31 mV), and Ru/WO_x-600 (50 mV) samples exhibited relatively higher overpotential. Especially, Ru/WO_3-V_O needs a low overpotential of 139 mV for the current density of 100 mA cm^{-2}. Ru/WO_3-V_O exhibits the lowest overpotential with 2.2 *wt*% Ru (Fig. S1a). Comparatively, the higher overpotential of commercialized Pt/C (21 mV), Ru/C (31 mV), and Ru (50 mV) catalysts demonstrated Ru/WO_3-V_O as an excellent candidate (Fig. 1b).

Tafel slope was adopted to discriminate kinetic process and reaction mechanism of Ru/WO_3-V_O. In Fig. 1c, the Tafel slope of RuO_2/WC, WC, commercial Ru, Ru/C, Pt/C and Ru/WO_3-V_O are 135.8, 92.3, 71.1, 64.6, 39.4 and 35.8 mV dec^{-1}, respectively. The low Tafel slope proposes Volmer-Tafel reaction pathway for Ru/WO_3-V_O [34,35]. To understand the kinetics of Ru/WO_3-V_O, the exchange current density (j_0) was obtained by extrapolating Tafel plot. The j_0 value of Ru/WO_3-V_O (5.26 mA cm^{-2}) is larger than that of Ru/C and Pt/C (Fig. S1b). The minimum driving force was required for the HER reaction on Ru/WO_3-V_O because of the maximum j_0 value [36]. The intrinsic activity of Ru/WO_3-V_O is further demonstrated by the Tafel slopes and corresponding overpotential of Ru/C and Pt/C at 10 mA cm^{-2} (Fig. S1c). Furthermore, comparison with the recently reported catalyst, Ru/WO_3-V_O exhibited excellent HER performance with a low overpotential value [37–39]. The leading position of Ru/WO_3-V_O is confirmed by the comparison with the recently reported HER catalysts (Table S1).

KSCN shielding effect was employed to reveal the active sites in Ru/WO_3-V_O. In Fig. S4d and S1e, current density of Ru/WO_3-V_O electrocatalyst exhibited a sharp decrease after the addition of SCN^- ions because of the rapid deactivation of metal active sites in Ru/WO_3-V_O. At the same time, overpotential of Ru/WO_3-V_O increased from 10 to 128 mV at the current density of 10 mA cm^{-2} because of the low active of metal active sites. Similarly, current density decreases from 146 to 28 mA cm^{-2} at overpotential of 200 mV (Fig. S1f). According to the above results, the ratio of contribution to current from Ru metal and non-metal active sites in Ru/WO_3-V_O are 81 % and 19 %, respectively [36]. Besides metal active sites, non-metal active sites also exist in WO_3 phase [40].

To compare the concentration of active sites of Ru/WO_3-V_O, ECSA was evaluated. the higher active site concentration of Ru/WO_3-V_O (53.7 mF cm^{-2}) was indicated by the C_{dl} (Ru/C: 42.6, Pt/C: 41.2, RuO_2/WC precursor: 7.8 mF cm^{-2}, Fig. 1d) and ECSA value (Table S2). Furthermore, in the electrochemical impedance spectroscopy (EIS) (Fig. 1e), the charge transfer resistance of Ru/WO_3-V_O (6.5 Ω) is smaller than that of Pt/C (9.7 Ω), RuO_2/WC (38.5 Ω), Ru/C (11.9 Ω), Ru (15.0 Ω), and WC (48.9 Ω). The low resistance signifies the efficient charge transfer ability of Ru/WO_3-V_O [41]. The *TOF* values of Ru/WO_3-V_O electrocatalyst are much larger than those of commercial Pt/C and Ru/C at different overpotential (Fig. 1f). Especially, at overpotential of 100 mV, the *TOF* of Ru/WO_3-V_O (6.1 s^{-1}) is 7.2 and 9.1 times higher than that of commercial Pt/C (0.84 s^{-1}) and Ru/C (0.67 s^{-1}), respectively. The TOF values of Ru/WO_3-V_O with other Ruthenium-based materials reported recently were listed in Table S3. High *TOF* value can better understand the intrinsic activity and application potential of Ru/WO_3-V_O.

The HER performances of Ru/WO_3-V_O under different pH (0−14) conditions were further studied. The low overpotential is 53 and 65 mV in pH = 7 and pH = 0 solutions at current density of 10 mA cm^{-2} (Fig. S2a), respectively. Corresponded Tafel slopes were calculated as 50.2 and 66.3 mV dec^{-1} (Fig. S2b, c), respectively. Small overpotential and Tafel slopes difference means better pH applicability. The excellent HER performance under both acidic and neutral conditions is beneficial for the application in proton exchange membranes and microbial electrolyzes [42]. The similar C_{dl} values at different pH mean stable electrode active area of Ru/WO_3-V_O (Fig. S2d-f). The stable charge transfer ability of Ru/WO_3-V_O is proposed by the R_{ct} values of 12.0 and 13.1 Ω under acidic and neutral conditions, respectively (Fig. S2g). *TOF* values and mass activity of Ru/WO_3-V_O under acidic and neutral conditions suggest more HER active sites exposed for Ru/WO_3-V_O (Fig. S2h and Fig. S2i). Ru/WO_3-V_O shows higher mass activity than Pt/C and Ru/C after normalized by the precious metal mass. (Fig. S3). The almost unchanged polarization curves of Ru/WO_3-V_O before and after 10,000 cycles under different pH (0−14) conditions demonstrated excellent cycling stability in a wide pH range (Fig. 1g).

In chronopotentiometry test under a constant current density of 50 mA cm^{-2}, the voltage on Ru/WO_3-V_O was nearly constant during 60 h in 1 M KOH (Fig. S4a). After 10 h at an initial current density of 220 mA cm^{-2}, there is still 92 % current retention (Fig. S4b). Ru/WO_3-V_O still showed the strong stability at higher current. In addition, step potential i-t test during 20 h also confirmed the good stability of Ru/WO_3-V_O (Fig. S4c) in 1 M KOH. The TEM and HRTEM images of Ru/WO_3-V_O catalyst after 10,000 cycles test for HER in alkaline solution was shown in Fig. S5. It is clearly that the hetero-structure of Ru/WO_3-V_O after test was still maintained, which is similar to that of catalyst before test. XAFS results in Fig. S6 suggest that the chemical state of W still maintains the structure of WO_3 and no obvious change after cycling. The peak around 1.31 Å was assigned to the signals of W–O shell of Ru/WO_3-V_O after 10,000 cycles test. The characteristic peak of Ru–Ru coordination in Ru/WO_3-V_O after 10,000 cycles test is conformed at 2.35 Å. Compared with the path of Ru-Ru bond (2.42 Å) in Ru foil, it is basically consistent. It shows that the metal structure of Ru remains unchanged in Ru/WO_3-V_O after 10,000 cycles test. In addition, the existence of the Ru–O coordination peak is due to slight oxidation occurred on the surface of Ru/WO_3-V_O during the collection process. The well-maintained original structural characteristics after long cycling indicated the excellent structural stability of Ru/WO_3-V_O. Long-term i-t test of Ru/WO_3-V_O in 0.5 M H_2SO_4 exhibited a slight current density decay (Fig. 1h). The above experimental results also proved the strong stability of Ru/WO_3-V_O in a wide pH range. The Faradaic efficiency of Ru/WO_3-V_O for HER was determined by quantifying the volume of the generated H_2 at 100 mA. The evolution of the Faradaic efficiency for H_2 was close to 100 % (Fig. S7). It delivers the yield rates of 1770 μmol cm^{-2} h^{-1} for H_2 It delivers the yield rates of 1770 μmol cm^{-2} h^{-1} for H_2. The unprecedented catalytic activity of Ru/WO_3-V_O for HER may originate from the synergistic effect between the mixed phase WO_3-V_O and the metallic Ru.

3.2. The SPR synthesis and mechanism

RuO_2/WC precursor was sealed in a furnace and to anneal under Ar atmosphere for the exploration of SPR synthesis (Fig. 2a). XRD was adopted to track SPR process and illustrate phase transformation of RuO_2/WC. The ex-situ variable temperature XRD patterns of RuO_2/WC (Fig. 2b) demonstrate that the signal of WC gradually disappeared after thermal treatment [43]. Consequently, new-formed crystalline WO_3 (JCPDS: 71–2141) was observed above 400 °C [21]. The sharper diffraction peaks of WO_3 at 600 °C reveal a higher crystallinity than those of lower temperature. The XRD of RuO_2/WC after annealing at different temperatures also illustrate a weak crystallinity of Ru/WO_3 annealed at 450 °C (Fig. S8). Meanwhile, the crystal phase of WO_3 gradually changes from monoclinic to orthorhombic with rising temperature. The diffraction peaks of Ru are relatively weak (JCPDS: 06–0663), because of its low content in RuO_2/WC [44]. These results indicated that WC and RuO_2 are simultaneously converted into WO_3 and Ru metal during the annealing process. The first 2.8 % weight loss before 100 °C in TGA is ascribed to the removal of water molecules adsorbed on

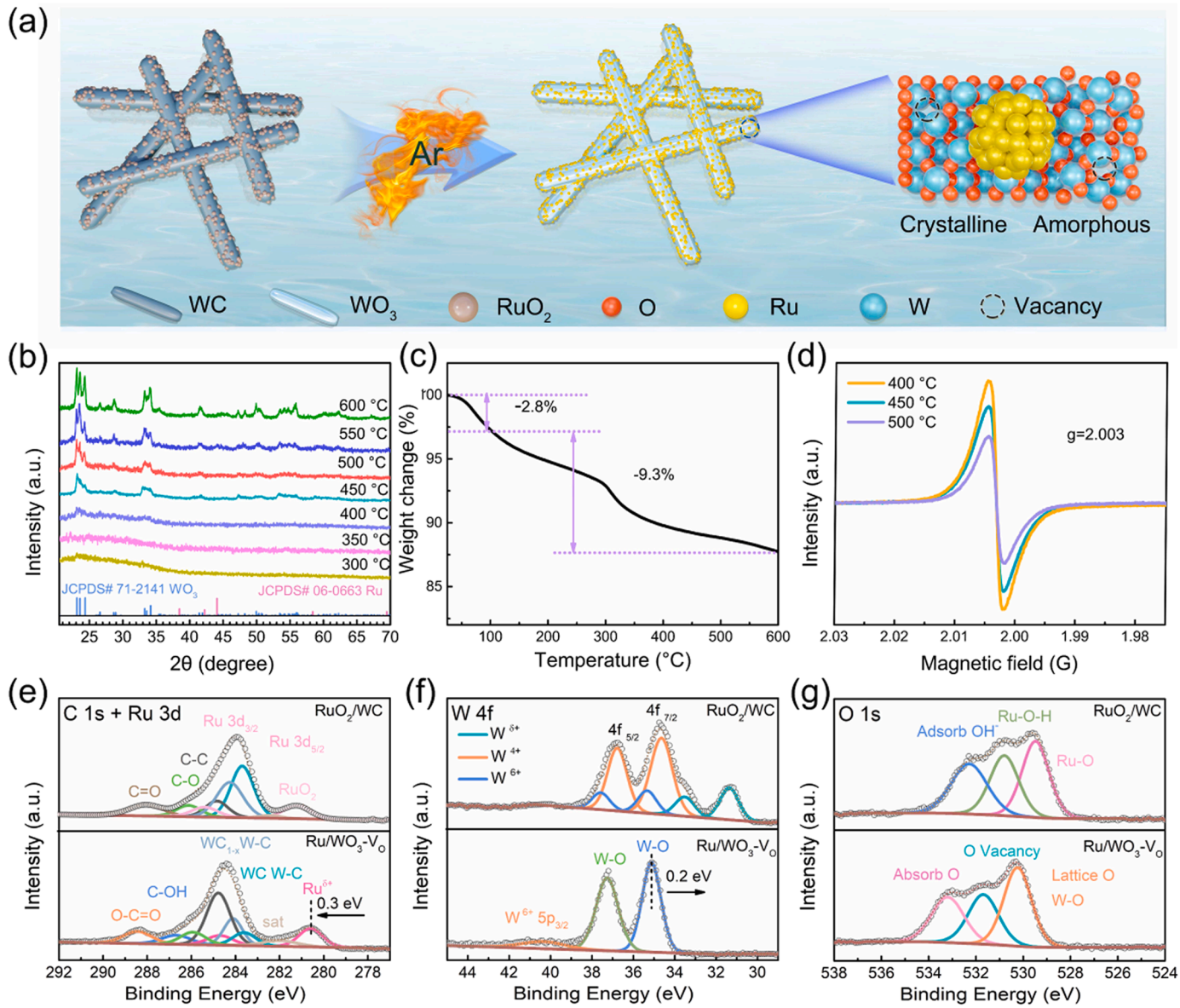

Fig. 2. (a) The fabrication process of Ru/WO_3-V_O. (b) Ex-situ variable temperature XRD patterns of as-constructed RuO_2/WC precursor sample. (c) TGA curves of RuO_2/WC precursor. (d) EPR spectra for RuO_2/WC precursor at different temperatures. XPS spectra of RuO_2/WC and Ru/WO_3-V_O, (e) Ru 3d, (f) W 4 f and (g) O 1 s.

the surface of RuO_2/WC (Fig. 2c) [44]. There is a slow weight loss between 100 and 300 °C and a rapid weight loss between 300 and 350 °C. Furthermore, the weight loss rate becomes slower again in the range of 350–600 °C. The total weight loss in the range of 100 ~ 600 °C implies an annealing process of RuO_2/WC with gas release. As shown in Fig. S9, the clarified lime water becomes to be turbid after the introduction of tail gas, indicating the generation of CO_2 in the annealing process. The SPR process starting at 100 °C is relatively slow below 300 °C. WC and RuO_2 are quickly converted into WO_3 and Ru metal simultaneously from 300 °C to 350 °C. The reaction rate also slows down as temperature exceeds 350 °C because of the decreasing reactants. The transformation starts at 400 °C from amorphous WO_3 phase to crystalline WO_3 phase [19]. Because CO_2 gas is easily release during SPR process, the generated anion vacancies can accelerate the mobility of lattice oxygen to promote the generation of V_O in new-formed amorphous/crystalline WO_3 phase.

The V_O in new-formed amorphous/crystalline WO_3 phase was tracked by EPR of RuO_2/WC after annealing at different temperatures. As shown in Fig. 2d, the presence of V_O is confirmed by the strong signal of V_O with a *g*-factor of 2.003 [45,46]. The intensity of V_O signal gradually weakens with the increase of annealing temperature from 400 °C to 500 °C. The decrease in V_O concentration is attributed to increasing reaction temperature of SPR. Concentrated V_O is induced by abundant defects in the lattice of WO_3 [25]. Therefore, appropriate reaction temperature of RuO_2/WC to obtain Ru/WO_3 composite with concentrated V_O is in the range of 400–500 °C. The bonding states of the elements in RuO_2/WC and Ru/WO_3-V_O was investigated by XPS. As shown in Fig. 2e, the Ru^{4+} spectra was disappeared and metallic Ru was generated in Ru/WO_3-V_O [47]. At the same time, the binding energy of both the Ru $3d_{5/2}$ ($Ru^{\delta+}$ 280.5 eV) and W 4 $f_{7/2}$ (W^{6+} 35.1 eV) peaks have offset in different directions. As shown in Fig. 2f, a shift of 0.2 eV lower than W^{6+} in RuO_2/WC is found, which is due to the little part of WC oxidized by H_2O_2. Also, a shift of 0.3 eV higher than Ru^0 is found in Ru/WO_3-V_O [45,48,49]. The lower work function metallic Ru than WO_3 causes the electron transfer from Ru to WO_3 by reducing the electron energy. In high-resolution O 1s spectrum of Ru/WO_3-V_O (Fig. 2g), the lattice oxygen (Ru–O) at 529.5 eV was disappeared compared with RuO_2/WC [36]. The peak can be deconvoluted into three components, with peaks at 530.0, 531.7 and 533.2 eV, and assigned to lattice oxygen

(W–O), oxygen vacancies, and adsorbed oxygen in the Ru/WO_3-V_O [24,25,50]. Oxygen vacancies is also confirmed by the signal appearing in EPR curve.

3.3. Structure feature

Structural information of Ru/WO_3-V_O was revealed by SEM and TEM. As-constructed WC material showed a uniform one-dimensional rod-like structure with an average size about 25 nm (Fig. S10). The lattice spacing of 0.25 nm was corresponded to the (100) plane of WC (Fig. S11) [51,52]. The rod-like shape of Ru/WO_3-V_O is similar to that of WC. A large number of RuO_2 NPs were coated with nanorods (Fig. 3a). Tiny Ru metal NPs are uniformly distributed onto WO_3 nanorods without obvious agglomeration. The Ru NPs uniformly with an average

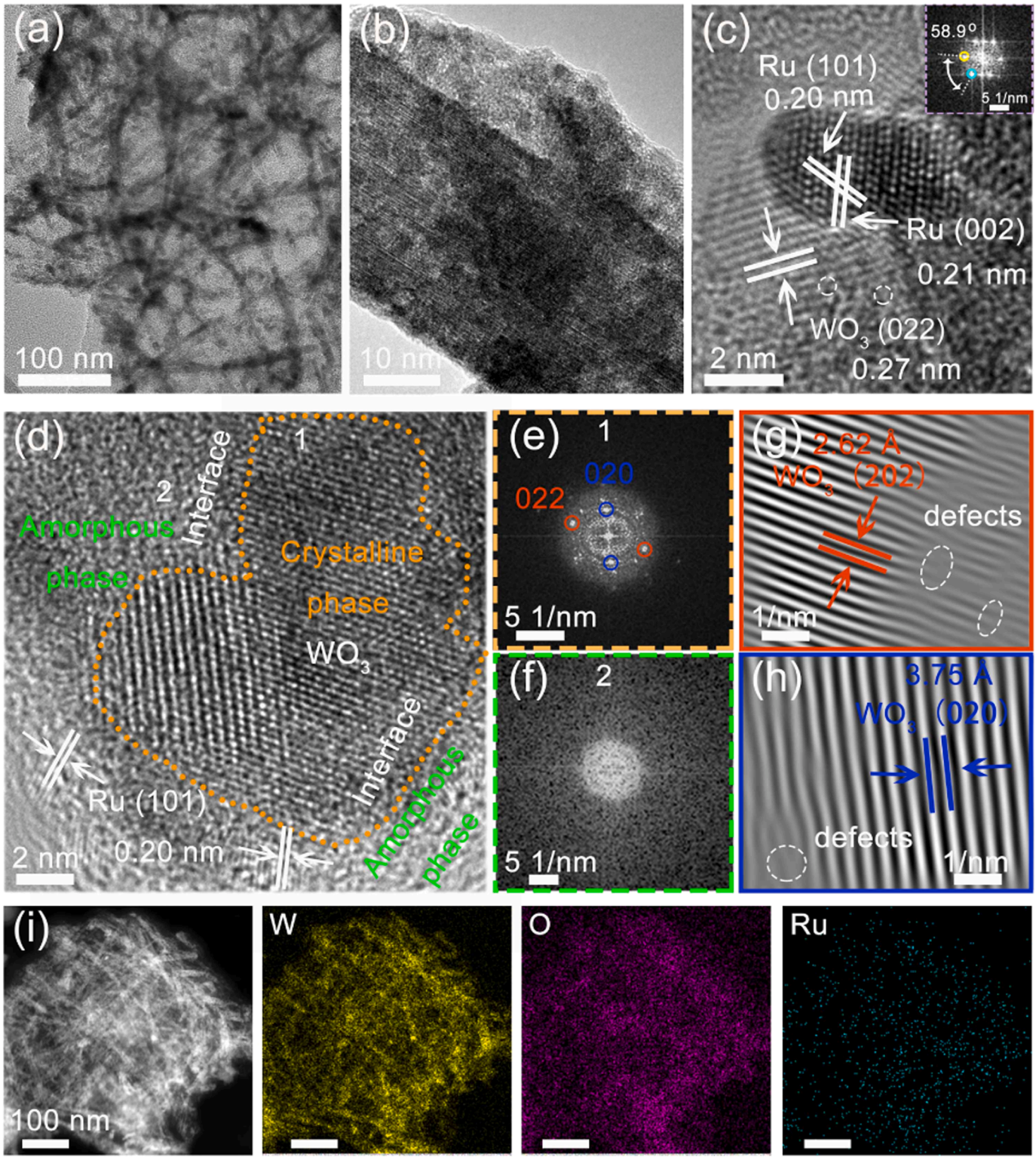

Fig. 3. (a, b) TEM images of Ru/WO_3-V_O. (c) HRTEM images and their corresponding SAED pattern patterns Ru/WO_3-V_O. (d-h) HRTEM images and their corresponding FFT patterns of Ru/WO_3-V_O. (i) EDX mapping images of W, Oand Ru.

size of 2.2 nm (Fig. S12a,b). The lattice spacing of 0.21 and 0.20 nm were corresponded to the (101) and (002) planes of Ru, respectively (Fig. 3b) [20,53]. The lattice spacing of 0.27 nm was ascribed to the (022) plane of WO_3 phase [54]. Significantly, the lattice deletions and structure distortions observed in the adjacent WO_3 phase suggest a partial amorphization of WO_3. Therefore, WO_3 is an amorphous/crystalline heterostructure.

In the fast Fourier transform (FTT) map of Ru region (Fig. 3c), the angle between (101) and (002) crystal planes about 58.9° represent a hexagonal closest-packed (hcp) structure of generated Ru metal [53]. the interface between crystalline and amorphous WO_3 is obvious in Ru/WO_3-V_O (Fig. 3d and Fig. S12c,d)). The right part displays fine diffraction fringes. The lattice spacing of 3.75 Å and 2.62 Å were ascribed to (022) and (202) plane of crystalline WO_3, respectively [55, 56]. In contrast, the discontinuous lattice fringes in left part suggest the presence of V_O rich in-amorphous WO_3 phase. The corresponding FTT maps also illustrated the difference between crystalline phase (visible diffraction spots, Fig. 3e) and amorphous phase (diffraction halos and no visible diffraction spots, Fig. 3f). The identifiable diffraction spots are corresponding to the (022) (Fig. 3g) and (020) (Fig. 3h) planes of crystalline WO_3 [44]. EDX results of HAADF-STEM (Fig. 3i) revealed the uniformly distribution of W, O, and Ru elements in Ru/WO_3-V_O.

The coordination environment and electronic structure of RuO_2/WC and Ru/WO_3-V_O was analyzed by X-ray absorption near-edge structure (XANES) and extended X-ray absorption fine structure (EXAFS). In W L_3 edge XANES spectrum of Ru/WO_3-V_O (Fig. 4a), the intensity of the white line peak is lower than that of the standard sample WO_3. The average oxidation valence state of W element in Ru/WO_3-V_O is not standard

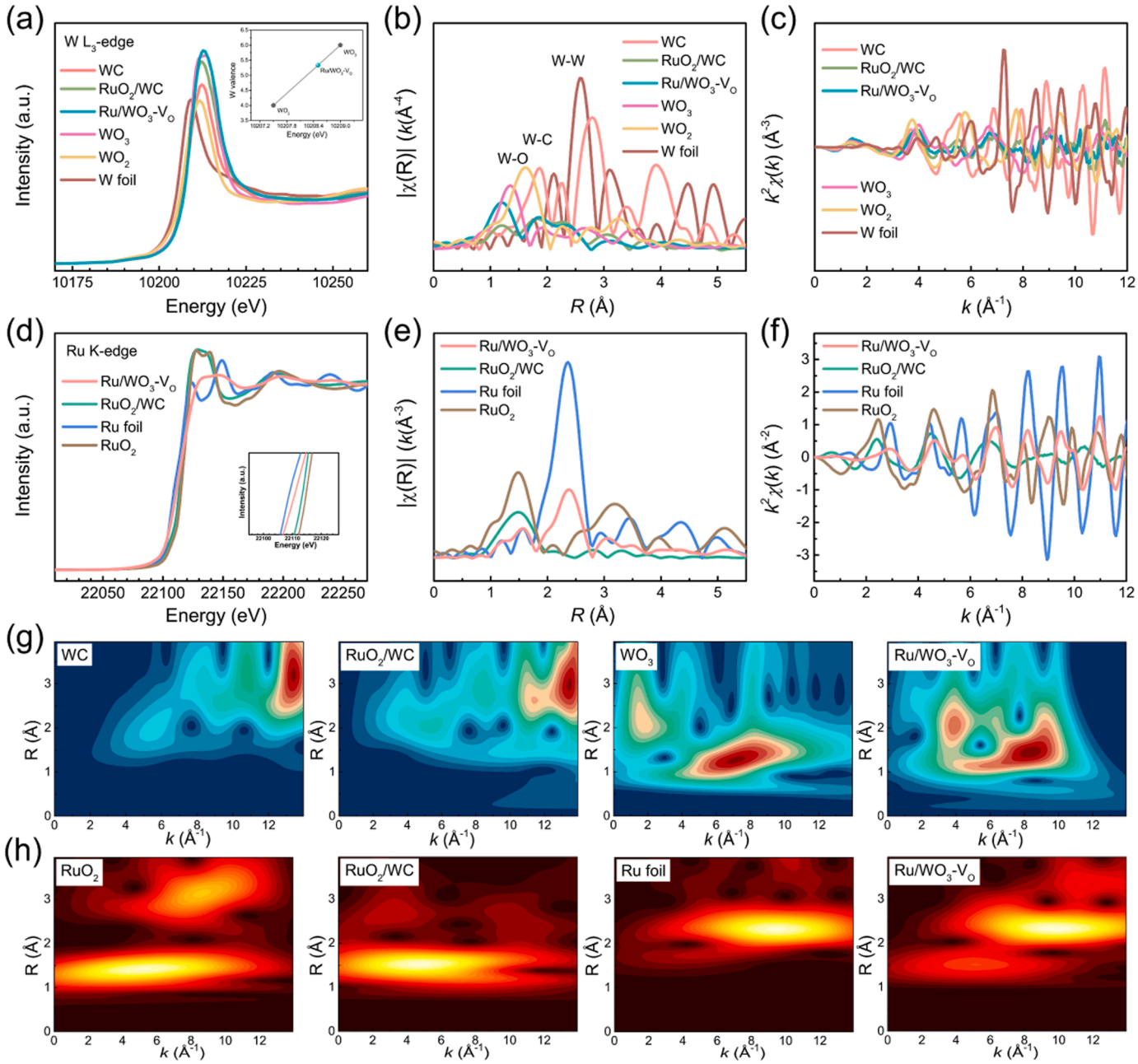

Fig. 4. (a) XANES of W L_3-edge of Ru/WO_3-V_O and RuO_2/WC with standard WO_2, WC and WO_3 as references. (b) EXAFS spectrum in *R* space and (c) EXAFS oscillations in *k*-space. (d) XANES of Ru K-edge of Ru/WO_3-V_O and RuO_2/WC with Ru metal foil and RuO_2 as references. (e) EXAFS spectrum in *R* space and (f) EXAFS oscillations in *k*-space (g) The W L_3-edge WT-EXAFS of the WC, Ru/WO_3-V_O, and standard MoO_2. (h) The Ru K-edge WT-EXAFS of the Ru/WO_3-V_O, RuO_2/WC, RuO_2, Ru foil.

W^{6+}, but lower than + 6 valence [57]. Fitting the first and second coordination shell from the W L3-edge extended EXAFS curve of Ru/WO_3-V_O and standard WO_3 (Fig. S13). The W–O coordination numbers of the two structures of WO_3 are about 6, which are 3.3 and 2.7 coordination, respectively. The two W–O coordination numbers of Ru/WO_3-V_O are about 4.8, which are 1.9 and 2.9 coordination, respectively. This is due to the large number of oxygen vacancies in Ru/WO_3-V_O leading to a decrease oxygen coordination number. The valence state of Ru/WO_3-V_O was analyzed by linear fitting. The average valence state of the W element was + 5.3, which was caused by the presence of oxygen vacancies and amorphous phase in the WO_3 In Fig. 4b, the characteristic peak of W–C and W–W coordination in RuO_2/WC is conformed at 1.82 and 2.27 Å, respectively [58]. In Ru/WO_3-V_O, the typical W–O shell signal peak at 1.22 Å confirms the conversion of WC to WO_3 [58].

The absorption edge energy of Ru K-edge XANES spectrum in Ru/WO_3-V_O slightly higher than that of standard Ru foil is much lower than that of standard RuO_2 and RuO_2/WC (Fig. 4d). In Fig. 4e, Ru–Ru coordination (2.37 Å) in Ru/WO_3-V_O is close to that of Ru foil [59]. EXAFS oscillation spectra of Ru/WO_3-V_O at Ru K-Edge k space is similar to that of standard Ru (Fig. 4f). These results indicated the successful transformation of RuO_2 to Ru elemental after the SPR process. Compared to EXAFS oscillation spectra of standard WO_3 at W L_3-Edge k space (Fig. 4c), the oscillation curve of Ru/WO_3-V_O (Fig. 4c) is similar. The significant decrease in amplitude of the Ru/WO_3-V_O represent local atomic arrangements of Ru/WO_3-V_O different from standard WO_3 [60]. The possible reason for this phenomenon is the existence of amorphous phase and V_O in Ru/WO_3-V_O. The wavelet transform (WT) plot of R-space and k-space of the W L_3-edge of WC, WO_3, RuO_2/WC, and Ru/WO_3-V_O was shown in Fig. 4g. The WT showed the dispersion of atomic positions in the radial distance and k-space at high resolution, more intuitive to distinguish the phase information. In Ru/WO_3-V_O, the maximum intensity near $k = 8.2$ Å^{-1} is attributed to the W–O coordination, while the intensity at $k = 3.9$ Å^{-1} originates from the W–W coordination [58]. The WT signal in Ru/WO_3-V_O is significantly different from the W–W bond in RuO_2/WC (~13.5 Å^{-1}) and WC (~13.4 Å^{-1}). In Fig. 4h, the peak of Ru shell in Ru/WO_3-V_O at $k = 9.6$ Å^{-1} is assigned to Ru-Ru coordination, close to the Ru–Ru coordination of Ru foil ($k = 9.4$ Å^{-1}) [36]. These results also confirmed the successful transformation of RuO_2 and WC into Ru and WO_3 after SPR process.

As shown in Fig. 2b and S5, RuO_2 and WC in RuO_2/WC at room

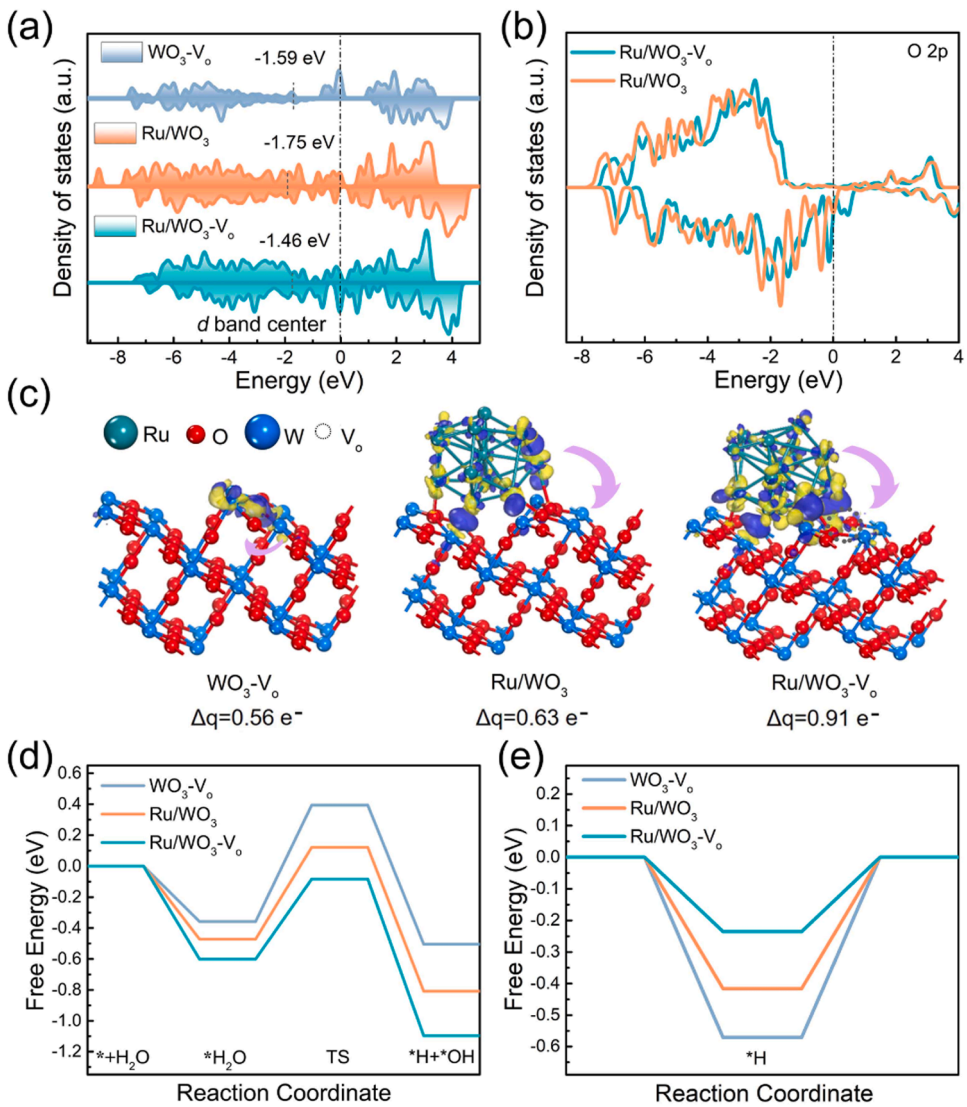

Fig. 5. (a) Total-density-of-states, the *d*-band center and (b) partial density of states of the O 2p orbital of WO_3-V_O, Ru/WO_3, and Ru/WO_3-V_O. (c) Electron density difference plot across the Ru/WO_3 and Ru/WO_3-V_O. (d) the corresponding free-energy diagram of H_2O dissociation reaction toward alkaline HER and (e) Gibbs free energy diagrams for H adsorption on WO_3-V_O, Ru/WO_3, and Ru/WO_3-V_O.

temperature are inert. As temperature rises, the redox reaction drives RuO_2 and WC to transform into Ru metal and WO_3. When reaction temperature is controlled in a fine range (400–500 °C), the appropriate reaction rate and restricted motion behavior of atoms in solid state precursor promote the generation of tremendous Vo in new-formed crystalline/amorphous WO_3 phase (WO_3-Vo). The synergistic effect between V_O and Ru can tune the electronic properties of Ru/WO_3-V_O to accelerate the interfacial charge transfer. The optimized *d*-band center will enhance the total electrochemical activity [61].

3.4. Catalytic mechanism

DFT calculations were used to reveal the catalytic mechanism of Ru/WO_3-V_O in theoretical perspective. Three catalytic structural models (WO_3-V_O, Ru/WO_3, and Ru/WO_3-V_O) were constructed, where WO_3 (022) and Ru (101) planes were chosen for the study (Fig. S14). A total density of states (TDOS) study is continuously performed near the Fermi level [25]. The highest TDOS value of Ru/WO_3-V_O model at the Fermi level implise more metallic than those of WO_3-V_O and Ru/WO_3 in Fig. 5a. The high conductivity is beneficial for charge transfer in HER process [62]. The *d*-band center (εd) of WO_3-V_O, Ru/WO_3 and Ru/WO_3-V_O (Fig. 5a) are located at –1.59, –1.75, and –1.46 eV, respectively. Compared to WO_3-V_O and Ru/WO_3, εd position of Ru/WO_3-V_O mode close to Fermi level with beneficial for promoting the interaction between reaction intermediates and catalyst. The shifted projected density of state (PDOS) of O 2p in Ru/WO_3-V_O cause the energy band center approach Fermi energy level compared to Ru/WO_3 (Fig. 5b). Due to the existence of V_O in Ru/WO_3-V_O, the adsorption behavior of reactants on the catalyst surface and the reaction energy barrier were also optimized.

The charge distribution in WO_3-V_O, Ru/WO_3, and Ru/WO_3-V_O is revealed by Electron density difference (EDIFF). The yellow and blue color areas present the accumulation and dissipation of electrons, respectively. The electrons transfer from Ru metal to WO_3 in Ru/WO_3 and Ru/WO_3-V_O in Fig. 5c. The significantly enhanced charge accumulation density of WO_3 in Ru/WO_3-V_O implies that V_O in WO_3 accelerates the charge redistribution and electron transfer from Ru to WO_3 [63]. The V_O can improve the interaction between Ru and WO_3. The facilitated adsorption of reaction intermediates and desorption of products enhance the overall activity of Ru/WO_3-V_O. The above results illustrated that Ru/WO_3-V_O owns the optimal electronic structure among these three catalytic models.

Fig. 5d shows free energy diagrams of HER reaction steps in catalyst models WO_3-V_O, Ru/WO_3, and Ru/WO_3-V_O. Compared to acidic electrolyte, initial water dissociation process was needed in Volmer step of alkaline HER·H_2O supplies H* to following steps by cleaving H–OH bond (Fig. S15) [61,62]. Ru/WO_3-V_O exhibits much lower H_2O adsorption energy of –0.60 eV than those of Ru/WO_3 (–0.47 eV) and WO_3-V_O (–0.36 eV) for its excellent H_2O adsorption kinetics. In Ru/WO_3-V_O catalyst model, H_2O molecules are first adsorbed onto Ru sites. The V_O and adjacent W metal active sites jointly induce the dissociation of H_2O molecule·H_2O molecular dissociation energy barrier of Ru/WO_3-V_O is 0.51 eV, lower than those of WO_3-V_O (0.75 eV) and Ru/WO_3 (0.59 eV). This result reveals that the synergistic effect between WO_3-V_O and Ru can significantly reduce the energy barrier of water dissociation. The free energy of hydrogen adsorption (ΔG_{H^*}) on Ru/WO_3-V_O surface is 0.23 eV (Fig. 5e), near the thermo neutral value compared to WO_3-V_O (0.57 eV) and Ru/WO_3 (0.42 eV) [61]. The appropriate ΔG_{H^*} value of Ru/WO_3-V_O is beneficial for accelerating the departure of H* and re-exposing the active site [61]. Therefore, the excellent HER performance of Ru/WO_3-V_O is attributed to the cooperation of WO_3-V_O and Ru metal.

4. Conclusions

In conclusion, crystalline/amorphous semiconductor-metal heterostructures by an SPR strategy were demonstrated to be outstandingly active for HER in a wide pH range. In Ru/WO_3-V_O, plenty of highly active tiny Ru NPs were decorated onto the outer surface of WO_3-V_O nanorods. Tremendous of active sites and unique amorphous/crystalline phase is responsible for the HER performance and stability of Ru/WO_3-V_O catalyst in alkaline, neutral, and acid medium. The ultralow overpotential of 10 mV as 10 mA cm^{-2} in 1 M KOH confirms the potential application of Ru/WO_3-V_O catalyst for pH-universal HER. DFT calculations demonstrated that synergistic effect between WO_3-V_O and Ru NPs results in enhanced electron transfer ability, tuned electronic structure, and high overall catalytic activity. The catalyst design through SPR strategy also provides a new idea for the design of the crystalline/amorphous semiconductor-metal heterointerface structure for efficient HER in sustainable energy.

CRediT authorship contribution statement

Jialin Cai: Investigation, Visualization, Writing – original draft, Writing – review & editing, Formal analysis. **Wenlei Zhang**: Investigation, Conceptualization, Supervision. **Yanyan Liu**: Investigation, Funding acquisition. **Ruofan Shen**: Investigation. **Xin Xie**: Investigation. **Wanyu Tian**: Investigation. **Xingang Zhang**: Investigation. **Jie Ding**: Investigation, Supervision. **Yushan Liu**: Visualization, Formal analysis, Supervision, Funding acquisition. **Baojun Li**: Formal analysis, Supervision, Conceptualization, Funding acquisition.

Declaration of Competing Interest

The authors declare that they have no known competing financial interests or personal relationships that could have appeared to influence the work reported in this paper.

Data Availability

Data will be made available on request.

Acknowledgments

This work was financially supported by the National Natural Science Foundation of China (Nos. 22279118, 21401168). The authors thank the Center for Modern Analysis and Gene Sequencing of Zhengzhou University in support of the characterization.

Supplementary material

Supplementary data associated with this article can be found, in the online version, at.

Appendix A. Supporting information

Supplementary data associated with this article can be found in the online version at doi:10.1016/j.apcatb.2023.123502.

References

[1] X. Chen, C. Li, M. Gratzel, R. Kostecki, S.S. Mao, Nanomaterials for renewable energy production and storage, Acc. Chem. Res. 41 (2012) 7909–7937, https://doi.org/10.1039/c2cs35230c.
[2] P. Hota, A. Das, D.K. Maiti, A short review on generation of green fuel hydrogen through water splitting, Int. J. Hydrog. Energy 48 (2023) 523–541, https://doi.org/10.1016/j.ijhydene.2022.09.264.
[3] S. Choi, J. Kwon, S. Jo, S. Kim, K. Park, S. Kim, H. Han, U. Paik, T. Song, Highly efficient and stable bifunctional electrocatalysts with decoupled active sites for hydrogen evolution and oxygen reduction reactions, Appl. Catal. B 298 (2021), 120530, https://doi.org/10.1016/j.apcatb.2021.120530.
[4] Y. Jiao, Y. Zheng, M. Jaroniec, S.Z. Qiao, Design of electrocatalysts for oxygen- and hydrogen-involving energy conversion reactions, Acc. Chem. Res. 44 (2015) 2060–2086, https://doi.org/10.1039/c4cs00470a.

[5] J. Xu, X. Kong, Amorphous/crystalline heterophase ruthenium nanosheets for pH-universal hydrogen evolution, Small Methods (2021), e2101432, https://doi.org/10.1002/smtd.202101432.
[6] M. Ling, N. Li, B. Jiang, R. Tu, T. Wu, P. Guan, Y. Ye, W.-C.M. Cheong, K. Sun, S. Liu, et al., Rationally engineered Co and N co-doped WS2 as bifunctional catalysts for pH-universal hydrogen evolution and oxidative dehydrogenation reactions, Nano Res. 15 (2021) 1993–2002, https://doi.org/10.1007/s12274-021-3898-6.
[7] H. Han, H. Choi, S. Mhin, Y.-R. Hong, K.M. Kim, J. Kwon, G. Ali, K.Y. Chung, M. Je, H.N. Umh, et al., Advantageous crystalline–amorphous phase boundary for enhanced electrochemical water oxidation, Energy Environ. Sci. 12 (2019) 2443–2454, https://doi.org/10.1039/c9ee00950g.
[8] T. Guo, P. Hu, L. Li, Z. Wang, L. Guo, Amorphous materials emerging as prospective electrodes for electrochemical energy storage and conversion, Chem 9 (2023) 1080–1093, https://doi.org/10.1016/j.chempr.2023.03.032.
[9] H. Jiang, T. Shang, H. Xian, B. Sun, Q. Zhang, Q. Yu, H. Bai, L. Gu, W. Wang, Structures and functional properties of amorphous alloys, Small Struct. 2 (2020), 2000057, https://doi.org/10.1002/sstr.202000057.
[10] Y. Zhai, X. Ren, J. Yan, S. Liu, High density and unit activity integrated in amorphous catalysts for electrochemical water splitting, Small Struct. 2 (2020), 2000096, https://doi.org/10.1002/sstr.202000096.
[11] Y. Zhang, F. Gao, D. Wang, Z. Li, X. Wang, C. Wang, K. Zhang, Y. Du, Amorphous/crystalline heterostructure transition-metal-based catalysts for high-performance water splitting, Coord. Chem. Rev. 475 (2023), https://doi.org/10.1016/j.ccr.2022.214916.
[12] J. Liang, Y. Ge, Z. He, Q. Yun, G. Liu, S. Lu, L. Zhai, B. Huang, H. Zhang, Wet-chemical synthesis and applications of amorphous metal-containing nanomaterials, Nano Res (2021), https://doi.org/10.1007/s12274-021-4007-6.
[13] P.F. Yin, M. Zhou, J. Chen, C. Tan, G. Liu, Q. Ma, Q. Yun, X. Zhang, H. Cheng, Q. Lu, et al., Synthesis of palladium-based crystalline@amorphous core-shell nanoplates for highly efficient ethanol oxidation, Adv. Mater. 32 (2020), e2000482, https://doi.org/10.1002/adma.202000482.
[14] N. Yang, H. Cheng, X. Liu, Q. Yun, Y. Chen, B. Li, B. Chen, Z. Zhang, X. Chen, Q. Lu, et al., Amorphous/crystalline hetero-phase Pd nanosheets: one-pot synthesis and highly selective hydrogenation reaction, Adv. Mater. 30 (2018), e1803234, https://doi.org/10.1002/adma.201803234.
[15] B. Jia, B. Zhang, Z. Cai, X. Yang, L. Li, L. Guo, Construction of amorphous/crystalline heterointerfaces for enhanced electrochemical processes, eScience 3 (2023), https://doi.org/10.1016/j.esci.2023.100112.
[16] J. Hu, S. Li, Y. Li, J. Wang, Y. Du, Z. Li, X. Han, J. Sun, P. Xu, A crystalline–amorphous Ni–Ni$(OH)_2$ core–shell catalyst for the alkaline hydrogen evolution reaction, J. Mater. Chem. A 8 (2020) 23323–23329, https://doi.org/10.1039/d0ta08735a.
[17] S. Liu, L. Dai, Y. Qu, Y. Qiu, J. Fan, X. Li, Q. Zhang, X. Guo, Crystalline/amorphous hetero-phase Ru nanoclusters for efficient electrocatalytic oxygen reduction and hydrogen evolution, Mater. Chem. Front. 5 (2021) 6648–6658, https://doi.org/10.1039/d1qm00812a.
[18] J. Liu, G. Qian, T. Yu, J. Chen, C. Zhu, Y. Li, J. He, L. Luo, S. Yin, Amorphous-crystalline heterostructure for simulated practical water splitting at high-current–density, Chem. Eng. J. 431 (2022), 134247, https://doi.org/10.1016/j.cej.2021.134247.
[19] Y. Shi, M. Sun, Y. Zhang, J. Cui, Y. Wang, X. Shu, Y. Qin, H.H. Tan, J. Liu, Y. Wu, Structure modulated amorphous/crystalline WO_3 nanoporous arrays with superior electrochromic energy storage performance, Sol. Energy Mater. Sol. Cells 212 (2020), 110579, https://doi.org/10.1016/j.solmat.2020.110579.
[20] R. Shen, Y. Liu, H. Zhang, S. Liu, H. Wei, H. Yuan, H. Wen, X. Wu, S. Mehdi, T. Liu, et al., Coupling oxygen vacancy and hetero-phase junction for boosting catalytic activity of Pd toward hydrogen generation, Appl. Catal. B 328 (2023), https://doi.org/10.1016/j.apcatb.2023.122484.
[21] E. Ozkan, S.-H. Lee, C.E. Tracy, J.R. Pitts, S.K. Deb, Comparison of electrochromic amorphous and crystalline tungsten oxide films, Sol. Energy Mater. Sol. Cells 79 (2003) 439–448, https://doi.org/10.1016/s0927-0248(03)00019-9.
[22] G.Y. Kim, K.R. Yoon, K. Shin, J.W. Jung, G. Henkelman, W.H. Ryu, Black tungsten oxide nanofiber as a robust support for metal catalysts: high catalyst loading for electrochemical oxygen reduction, Small 17 (2021), e2103755, https://doi.org/10.1002/smll.202103755.
[23] W. Liu, P. Jiang, Y. Xiao, J. Liu, A study of the hydrogen adsorption mechanism of $W_{18}O_{49}$ using first-principles calculations, Comput. Mater. Sci. 154 (2018) 53–59, https://doi.org/10.1016/j.commatsci.2018.07.036.
[24] Y. Niu, X. Teng, S. Gong, M. Xu, S.G. Sun, Z. Chen, Engineering two-phase bifunctional oxygen electrocatalysts with tunable and synergetic components for flexible Zn-Air batteries, Nano-Micro Lett. 13 (2021), 126, https://doi.org/10.1007/s40820-021-00650-2.
[25] J. Diao, W. Yuan, Y. Qiu, L. Cheng, X. Guo, A hierarchical oxygen vacancy-rich WO_3 with "nanowire-array-on-nanosheet-array" structure for highly efficient oxygen evolution reaction, J. Mater. Chem. A 7 (2019) 6730–6739, https://doi.org/10.1039/c9ta01044k.
[26] G. Zhuang, Y. Chen, Z. Zhuang, Y. Yu, J. Yu, Oxygen vacancies in metal oxides: recent progress towards advanced catalyst design, Sci. China Mater. 63 (2020) 2089–2118, https://doi.org/10.1007/s40843-020-1305-6.
[27] V.H.V. Quy, I.-R. Jo, S.-H. Kang, K.-S. Ahn, Amorphous-crystalline dual phase WO_3 synthesized by pulsed-voltage electrodeposition and its application to electrochromic devices, J. Ind. Eng. Chem. 94 (2021) 264–271, https://doi.org/10.1016/j.jiec.2020.10.047.
[28] W. Zhang, B. Huang, K. Wang, W. Yang, F. Lv, N. Li, Y. Chao, P. Zhou, Y. Yang, Y. Li, et al., WOx-surface decorated PtNi@Pt dendritic nanowires as efficient pH-universal hydrogen evolution electrocatalysts, Adv. Energy Mater. 11 (2020), 2003192, https://doi.org/10.1002/aenm.202003192.
[29] Y. Li, X. Zhai, Y. Liu, H. Wei, J. Ma, M. Chen, X. Liu, W. Zhang, G. Wang, F. Ren, et al., WO_3-based materials as electrocatalysts for hydrogen evolution reaction, Front. Mater. 7 (2020), 105, https://doi.org/10.3389/fmats.2020.00105.
[30] W. He, J. Chen, Q. Zhang, H. Cui, C. Wang, Tuning charge distribution of Ru nanoparticles via coupling ammonium tungsten bronze as Pt-Like electrocatalyst for hydrogen evolution reaction, Chem. Eng. J. 436 (2022), 135044, https://doi.org/10.1016/j.cej.2022.135044.
[31] F. Zhou, R. Sa, X. Zhang, S. Zhang, Z. Wen, R. Wang, Robust ruthenium diphosphide nanoparticles for pH-universal hydrogen evolution reaction with platinum-like activity, Appl. Catal. B 274 (2020), 119092, https://doi.org/10.1016/j.apcatb.2020.119092.
[32] J. Wang, B. Guo, J. Sun, Y. Zhou, C. Zhao, Z. Wei, J. Guo, Cooperative hydrogen evolution reaction combining $Cu_{2+1}O$ and Ru active sites, Appl. Catal. B 324 (2023), 122169, https://doi.org/10.1016/j.apcatb.2022.122169.
[33] J. Cai, J. Ding, D. Wei, X. Xie, B. Li, S. Lu, J. Zhang, Y. Liu, Q. Cai, S. Zang, Coupling of Ru and O^-vacancy on 2D Mo-based electrocatalyst via a solid-phase interface reaction strategy for hydrogen evolution reaction, Adv. Energy Mater. 11 (26) (2021), 2100141, https://doi.org/10.1002/aenm.202100141.
[34] H. Cheng, N. Yang, G. Liu, Y. Ge, J. Huang, Q. Yun, Y. Du, C.J. Sun, B. Chen, J. Liu, et al., Ligand-exchange-induced amorphization of Pd nanomaterials for highly efficient electrocatalytic hydrogen evolution reaction, Adv. Mater. 32 (2020), e1902964, https://doi.org/10.1002/adma.201902964.
[35] Y. Chen, R. Ding, J. Li, J. Liu, Highly active atomically dispersed platinum-based electrocatalyst for hydrogen evolution reaction achieved by defect anchoring strategy, Appl. Catal. B 301 (2022), 120830, https://doi.org/10.1016/j.apcatb.2021.120830.
[36] J. Cai, J. Yang, X. Xie, J. Ding, L. Liu, W. Tian, Y. Liu, Z. Tang, B. Liu, S. Lu, Carbon doping triggered efficient electrochemical hydrogen evolution of cross-linked porous Ru-MoO_2 via solid-phase reaction strategy, Energy Environ. Mater. 6 (2022), e12424, https://doi.org/10.1002/eem2.12424.
[37] D. Wang, X. Jiang, Z. Lin, X. Zeng, Y. Zhu, Y. Wang, M. Gong, G. Fu, Ethanol-induced hydrogen insertion in ultrafine IrPdH boosts pH-universal hydrogen evolution, Small 18 (2022), 2204063.
[38] Z. Wu, D. Nie, M. Song, T. Jiao, G. Fu, X. Liu, Facile synthesis of Co–Fe–B–P nanochains as an efficient bifunctional electrocatalyst for overall water-splitting, Nanoscale 11 (2019) 7506–7512.
[39] W. Li, H. Zhang, K. Zhang, W. Hu, Z. Cheng, H. Chen, X. Feng, T. Peng, Z. Kou, Monodispersed ruthenium nanoparticles interfacially bonded with defective nitrogen-and-phosphorus-doped carbon nanosheets enable pH-universal hydrogen evolution reaction, Appl. Catal. B 306 (2022), 121095.
[40] J. Park, S. Lee, H.E. Kim, A. Cho, S. Kim, Y. Ye, J.W. Han, H. Lee, J.H. Jang, J. Lee, Investigation of the support effect in atomically dispersed Pt on WO_{3-x} for utilization of Pt in the hydrogen evolution reaction, Angew. Chem. Int. Ed. 58 (45) (2019) 16038–16042, https://doi.org/10.1002/anie.201908122.
[41] G. Han, M. Hu, Y. Liu, J. Gao, L. Han, S. Lu, H. Cao, X. Wu, B. Li, Efficient carbon-based catalyst derived from natural cattail fiber for hydrogen evolution reaction, J. Solid State Chem. 274 (2019) 207–214, https://doi.org/10.1016/j.jssc.2019.03.027.
[42] J.-T. Ren, L. Chen, H.-Y. Wang, W.-W. Tian, X. Zhang, T.-Y. Ma, Z. Zhou, Z.-Y. Yuan, Inducing electronic asymmetricity on Ru clusters to boost key reaction steps in basic hydrogen evolution, Appl. Catal. B 327 (2023), 122466, https://doi.org/10.1016/j.apcatb.2023.122466.
[43] J. Diao, Y. Qiu, S. Liu, W. Wang, K. Chen, H. Li, W. Yuan, Y. Qu, X. Guo, Interfacial engineering of W2 N/WC heterostructures derived from solid-state synthesis: a highly efficient trifunctional electrocatalyst for ORR, OER, and HER, Adv. Mater. 32 (2020), e1905679, https://doi.org/10.1002/adma.201905679.
[44] K. Bao, S. Zhang, P. Ni, Z. Zhang, K. Zhang, L. Wang, L.X. Sun, W. Mao, Q. Zhou, Y. Qian, Convenient fabrication of carbon doped WO_{3-x} ultrathin nanosheets for photocatalytic aerobic oxidation of amines, Catal. Today 340 (2020) 311–317, https://doi.org/10.1016/j.cattod.2018.11.013.
[45] J. Chen, C. Chen, M. Qin, B. Li, B. Lin, Q. Mao, H. Yang, B. Liu, Y. Wang, Reversible hydrogen spillover in Ru-$WO_{(3-x)}$ enhances hydrogen evolution activity in neutral pH water splitting. Nat. Commun. 13 (2022), 5382 https://doi.org/10.1038/s41467-022-33007-3.
[46] R. Shen, Y. Liu, H. Wen, T. Liu, Z. Peng, X. Wu, X. Ge, S. Mehdi, H. Cao, E. Liang, et al., Engineering V_O-Ti ensemble to boost the activity of Ru towards water dissociation for catalytic hydrogen generation, Appl. Catal. B 306 (2022), 121100, https://doi.org/10.1016/j.apcatb.2022.121100.
[47] Y. Liu, H. Wen, D. Zhou, X. Huang, X. Wu, J. Jiang, X. Guo, B. Li, Tuning surface d charge of Ni-Ru alloys for unprecedented catalytic activity towards hydrogen generation from ammonia borane hydrolysis, Appl. Catal. B 291 (2021), 120094, https://doi.org/10.1016/j.apcatb.2021.120094.
[48] J. Shan, T. Ling, K. Davey, Y. Zheng, S.Z. Qiao, Transition-metal-doped ruir bifunctional nanocrystals for overall water splitting in acidic environments, Adv. Mater. 31 (2019), e1900510, https://doi.org/10.1002/adma.201900510.
[49] A. Salah, L. Zhang, H. Tan, F. Yu, Z. Lang, N. Al-Ansi, Y. Li, Advanced Ru/Ni/WC@NPC multi-interfacial electrocatalyst for efficient sustainable hydrogen and chlor-alkali co-production, Adv. Energy Mater. 12 (2022), 2200332, https://doi.org/10.1002/aenm.202200332.
[50] X. Xie, S. Wang, Y. Zhang, J. Ding, Y. Liu, Q. Yan, S. Lu, B. Li, Y. Liu, Q. Cai, Facile construction for new core-shell Z-scheme photocatalyst GO/AgI/Bi_2O_3 with enhanced visible-light photocatalytic activity, J. Colloid Interface Sci. 581 (2021) 148–158, https://doi.org/10.1016/j.jcis.2020.07.128.

[51] C. Liang, L. Ding, C. Li, M. Pang, D. Su, W. Li, Y. Wang, Nanostructured WCx/CNTs as highly efficient support of electrocatalysts with low Pt loading for oxygen reduction reaction, Energy Environ. Sci. 3 (2010) 1121–1127, https://doi.org/10.1039/c001423k.
[52] M. Shi, Z. Jiang, B. Mei, Y. Li, F. Sun, H. Yu, Y. Xu, Tuning the hydrogen evolution performance of 2D tungsten disulfide by interfacial engineering, J. Mater. Chem. A 9 (2021) 7059–7067, https://doi.org/10.1039/d0ta10673a.
[53] K. Gao, Y. Wang, Z. Wang, Z. Zhu, J. Wang, Z. Luo, C. Zhang, X. Huang, H. Zhang, W. Huang, Ru nanodendrites composed of ultrathin fcc/hcp nanoblades for the hydrogen evolution reaction in alkaline solutions, Chem. Commun. 54 (2018) 4613–4616, https://doi.org/10.1039/c8cc01343h.
[54] L. Liang, Q. Chang, T. Cai, N. Li, C. Xue, J. Yang, S. Hu, Combining carbon dots with WO3-x nanodots for utilizing the full spectrum of solar radiation in photocatalysis, Chem. Eng. J. 428 (2022), 131139, https://doi.org/10.1016/j.cej.2021.131139.
[55] X. Jiang, H. Jang, S. Liu, Z. Li, M.G. Kim, C. Li, Q. Qin, X. Liu, J. Cho, The heterostructure of Ru_2P/WO_3/NPC synergistically promotes H_2 O dissociation for improved hydrogen evolution, Angew. Chem. Int. Ed. 60 (8) (2021) 4110–4116, https://doi.org/10.1002/anie.202014411.
[56] Y. Su, H. Zhang, P. Liang, K. Liu, M. Cai, Z. Huang, C.-A. Wang, M. Zhong, A new binder-free and conductive-additive-free TiO_2/WO_{3-W} integrative anode material produced by laser ablation, J. Power Sources 378 (2018) 362–368, https://doi.org/10.1016/j.jpowsour.2017.12.063.
[57] L.-N. Zhang, Y.-Y. Ma, Z.-L. Lang, Y.-H. Wang, S.U. Khan, G. Yan, H.-Q. Tan, H.-Y. Zang, Y.-g Li, Ultrafine cable-like WC/W_2C heterojunction nanowires covered by graphitic carbon towards highly efficient electrocatalytic hydrogen evolution, J. Mater. Chem. A 6 (2018) 15395–15403, https://doi.org/10.1039/c8ta05007d.
[58] W. Chen, J. Pei, C.T. He, J. Wan, H. Ren, Y. Wang, J. Dong, K. Wu, W.C. Cheong, J. Mao, et al., Single tungsten atoms supported on MOF-derived N-doped carbon for robust electrochemical hydrogen evolution, Adv. Mater. 30 (2018), e1800396, https://doi.org/10.1002/adma.201800396.
[59] J. Li, Y. Li, J. Wang, C. Zhang, H. Ma, C. Zhu, D. Fan, Z. Guo, M. Xu, Y. Wang, et al., Elucidating the critical role of ruthenium single atom sites in water dissociation and dehydrogenation behaviors for robust hydrazine oxidation-boosted alkaline hydrogen evolution, Adv. Funct. Mater. 32 (2022), 2109439, https://doi.org/10.1002/adfm.202109439.
[60] W. Liang, M. Zhou, X. Lin, J. Xu, P. Dong, Z. Le, M. Yang, J. Chen, F. Xie, N. Wang, et al., Nickel-doped tungsten oxide promotes stable and efficient hydrogen evolution in seawater, Appl. Catal. B 325 (2023), 122397, https://doi.org/10.1016/j.apcatb.2023.122397.
[61] X. Fan, C. Liu, M. Wu, B. Gao, L. Zheng, Y. Zhang, H. Zhang, Q. Gao, X. Cao, Y. Tang, Synergistic effect of dual active sites over Ru/α-MoC for accelerating alkaline hydrogen evolution reaction, Appl. Catal. B 318 (2022), 121867, https://doi.org/10.1016/j.apcatb.2022.121867.
[62] H.C. Fu, X.H. Chen, B. Yang, Y.H. Luo, T. Li, X.H. Wang, Q. Zhang, X.L. Li, N.B. Li, H.Q. Luo, Unveiling the in-situ hydrogen intercalation in Mo_2CO_x for promoting the alkaline hydrogen evolution reaction, Appl. Catal. B 332 (2023), 122739, https://doi.org/10.1016/j.apcatb.2023.122739.
[63] C. Li, H. Jang, M.G. Kim, L. Hou, X. Liu, J. Cho, Ru-incorporated oxygen-vacancy-enriched MoO_2 electrocatalysts for hydrogen evolution reaction, Appl. Catal. B 307 (2022), 121204, https://doi.org/10.1016/j.apcatb.2022.121204.